



## **A COMPUTATIONAL AND EXPERIMENTAL INVESTIGATION OF AIR FLOW AND CONTAMINANTS CONCENTRATION IN A LABORATORY WITH MIXING VENTILATION SYSTEM**

**Ala'a A. Mahdi<sup>1</sup>, Mohammed W. Khadim<sup>2</sup> and Ammar A. Mohammed Hassan<sup>3</sup>**

<sup>1</sup> Assistant professor, Mechanical Engineering Dep., Collage of Engineering, University of Babylon, Iraq. Email: [alaa.mahdi1959@gmail.com](mailto:alaa.mahdi1959@gmail.com)

<sup>2</sup> PhD, Mechanical Engineering Dep., Collage of Engineering, University of Kerbala, Iraq. Email: [maljibory71@yahoo.com](mailto:maljibory71@yahoo.com)

<sup>3</sup> M.Sc. student, Mechanical Engineering Dep., Collage of Engineering, University of Kerbala, Iraq. Email: [Ammarsh1992@yahoo.com](mailto:Ammarsh1992@yahoo.com)

<http://dx.doi.org/10.30572/2018/kje/090314>

### **ABSTRACT**

In this research an experimental and computational analysis under Iraqi climate of temperature distribution, velocity and contaminants concentration in the air-conditioned laboratory have been studied for two case studies. Case-I chosen internal combustion engine laboratory of dimensions (10.3 x 8.7 x 3.75) m with a different number of engines used in the experiments and Case-II chosen laboratory of chemical and petroleum products dimensions (3.7x3.6x3.3)m with different locations of the supply air terminal diffuser compared to the existing design situation. ANSYS FLUENT 14 used to simulate the model's laboratories for compared between the present practical work and numerical work results which are acquired by using RNG K- $\epsilon$  and SST k- $\omega$  models and found that the SST k- $\omega$  model more accurate. The SST (k-w) turbulence model were employed to solve the governing equations numerically with Reynold number 28,933 and validated by comparing the numerical results with experimental data, and this comparison gives a good agreement. The numerical results for case-I compared with experimental data, while for case-II, the numerical results compared with the standard value due to Iraqi cooling code and ASHRAE standards. The results showed that the mixing ventilation system is able to remove various types of pollutants effectively up to 90% in addition to providing human thermal comfort conditions with the effectively of heat removal up to 85% for the state of the internal combustion laboratory. The second case at laboratory of chemical and petroleum products when the supply air terminal diffuser in the same side, the results showed an increase in comfort conditions by up to 40%. Lastly, from the research, it was found that the pollutant transportation and distribution depend in general upon several factors such as type and location of contaminant source, building geometry, the arrangement of air terminal diffuser opening, and thermal/fluid boundary conditions for example flow rate. Numerical simulation of the velocity and diffusion fields in a conventional flow in laboratories is very useful in comprehending flow and diffusion patterns within different changes of the flow conditions.

**KEYWORDS:** Mixing ventilation, Indoor air quality, air distribution performance index, Numerical model, Iraqi cooling code.

## 1. INTRODUCTION

One of the greatest fundamental human desires is fresh air. It has been evaluated that people expend relatively much time in indoor buildings. That generates an elevated requirement for high-quality ventilation systems in buildings. The ventilation airflow rate is recognized as the main factor for evaluating the indoor air quality (Gery Einberg, 2005). Heating, ventilation and air conditioning (HVAC) is the technology of indoor and vehicular environmental comfort. Its goal is to provide thermal comfort and acceptable indoor air quality. HVAC system design is a sub discipline of mechanical engineering, based on the principles of thermodynamics, fluid mechanics, and heat transfer. Providing occupants comfort and healthy environment with the minimum use of energy is the ultimate purpose of heating, ventilating and air conditioning (HVAC) systems (Hideyuki Amai, 2016). The application of mixing ventilation (MV) was already systematically illustrated in 1899 by Boyle Son (Boyle et al., 1899). In the last hundred years, numerous studies have been carried out to improve the performance of mixing ventilation (Butler, 1873). The climate of Iraq is hot and dry in summer, cold and rainy in winter, where the temperature reaches -5 degrees Celsius sometimes and may reach 50 degrees Celsius in summer in July and August. The warm months months in Iraq are characterized by two types of wind, south and south-easterly winds, dry sand winds usually occurring between April and May. Another type of wind prevails over Iraq between June and September, which is called the north and north-west winds, which are also dry and moderate winds. From these climatic data, there is a significant difference in temperature between the summer and winter, even during the day. Therefore, the design of the buildings should be thermally considered by selecting the most critical conditions in terms of temperature and the like (Iraqi Heating Code, 2013). To enhance the quality of indoor air by three basic ways: control the source of contaminants, eject the contaminants from the indoor air by air cleaner and use outdoor air ventilation to dilute the concentrations of contaminants (Awbi, 2007). The reviews spanning the last 30 years reiterate indoor air pollution (IAP) to be a major impact on comfort, health, wellness and performance factors that contribute to indoor air pollution are ubiquitous, both in the outdoor contaminants brought into the indoors as well as the ever increasing sources that are indoors (Hossain, 2012).

## 2. EXPERIMENTAL WORK

Study the distribution of temperature, the concentration of pollutants and distribution of airflow were conducted by several tests using the mixing ventilation system. The tests carried out in the Iraq climate by computing heat transfer across walls; appraise the actual volume of the airflow and the supply temperature desirable to obtain the best ventilation. The effects of the people and the various heat sources were also taking into account under steady-state conditions. The objective of empirical study was carried out in the internal combustion engine laboratory at University of Kufa/College of engineering. The indoor environment dimensions of the laboratory studied are 10.3m × 8.7m × 3.75m, as shown in Fig. 1.

Table 1 lists the configuration of the tested laboratory that studied. The Practical tests were conducted in the actual ambient of the laboratory with temperatures rang of (43-51) and for pressure 1 bar in the city of Najaf at 30 July. The sampling unit contains five sections with different heights (0.4, 0.8, 1.1, 1.5, 1.8) m from ground which used to measure the parameters that are situated at (x= 6.2 m, z=3.75) for pole-1, (x= 3.5 m, z=3.75) for pole-2 and (x=4.4 m,

z=7.5) for pole-3. Doors and windows are closed during the test time to simulate the actual reality. The Iraqi standards for cooling were used in this work in addition to ANSI/ASHRAE Standard 62-2001. The lab was illuminated by eight sets of twin double-batten fluorescent lights, with the power consumption of each fluorescent lamp of 140W.

**Table 1. Description of the room configuration.**

Item	NO.	Size m			Heat (W)
		$\Delta x$	$\Delta y$	$\Delta z$	
Computer table	1	0.8	0.6	0.5	-
Diffuser	1	0.49	0.1	0.34	-
Door	1	0	2	2.5	-
Diesel engine	1	0.8	1.8	1.5	50
Exhaust grille	1	0.37	0.05	0.36	-
Gasoline engine	1	2.4	2	0.9	65
Lights	8	0.1	0.1	1.3	36 per light
Person	7	0.4	1.1	0.35	75 per person
Room	1	10.3	8.7	3.75	-
Table1	1	2.20	1.08	2.25	-
Table2	1	2.20	0.9	1.2	-
Table for teacher	1	0.7	0.6	1.2	-
Window	2	2.5	0	1.5	-

## 2.1. System of air terminal supply

To estimate the quality of indoor air and thermal environment, inlet velocity, the temperature of inlet air, and effective temperatures was calculate by several steps depending on ASHRAE research.

### 2.1.1. Cooling load ventilation air flow rate

The airflow rate requisite for cooling in summer, using standard air, is (Awbi, 2007):

$$Q = \frac{0.295q_{oe} + 0.132q_l + 0.185q_{ex}}{\rho c p \Delta t_{hf}} \quad 1$$

To calculate the conduction of heat ( $q_{ex}$ ), all heat transferred over window and walls to the room should be taken into account and the equation (2) used for this calculate.

$$Q = UA\Delta T \quad 2$$

$$U = \frac{1}{R} , R = \frac{1}{h_i} + \frac{\Delta x}{k} + \frac{1}{h_o} \quad 3$$

The walls of building in Iraq mostly consist of multi- materials as (cement, common brick and gypsum) and details of materials are presented in [Table 2](#).

**Table 2. Details of materials and its thickness for the side walls & ceil ([Glicksman and Chen, 2003](#)).**

No.	Material	Thickness (mm)			K W/m.k
		Wall	Ceil	Floor	
1	Brick	240	-	-	0.72
2	Gypsum	20	10		0.42
3	Cement	10 for inside , 20 for outside	50	10	0.72
4	Concrete	-	200	-	1.1
5	Wood	30	-	-	0.173
6	Tile (mozaiek)	50	50	50	1.6
7	Sup Bess	-	-	200	2.6
8	Glass	6	-	-	1

### 2.1.2. Temperature of air supply:

Equation (4) is applied to found the temperature of air supply ( $T_s$ ) employed in the empirical test ([Versteeg and Malalasekera, 1995](#)).

$$T_s = t_{sp} - \Delta t_{hf} - \frac{A_f * q_t}{0.584 * Q^2 + 1.208 * A * Q} \quad 4$$

Depending on Iraqi cooling code and ASHRAE standard, the heat flux per person is 75W, the variation of temperature from head to foot level can be supposed 3°C. The air change per hour (ACH) can be determined by utilizing equation (5), ([Awbi, 2007](#)).

$$ACH = (Q/V_{Room}) * 3600 \quad 5$$

The calculated value of flow rate ( $Q_s$ ) used in this study was 414 l/s, air temperature supply was 12 °C and air change per hour (ACH) was 5 and [Fig. 2](#) shows the inlet terminal configuration.

## 2.2. Contaminants source

The composition and quantity of the emissions from an engine depend mainly on the type and condition of the engine. Diesel and gasoline engines emit CO, CO<sub>2</sub> and SO<sub>2</sub> etc., which absorb heat fast but do not release it easily to nature. As a result, an increase in these particles increases the air temperature. Moreover, these particles are also harmful to human health ([Hossain, 2012](#)). Since this simulation discussed only the variation of indoor CO<sub>2</sub> concentration, the operating fluid is only set as air and CO<sub>2</sub>. [Fig. 3](#) show selected internal combustion engine tested

laboratory for measurements. The mass fraction of CO<sub>2</sub> is set as 0.01135267 (Chen and Glicksman, 2003), and the other concentration types of contaminating are discussed numerically.

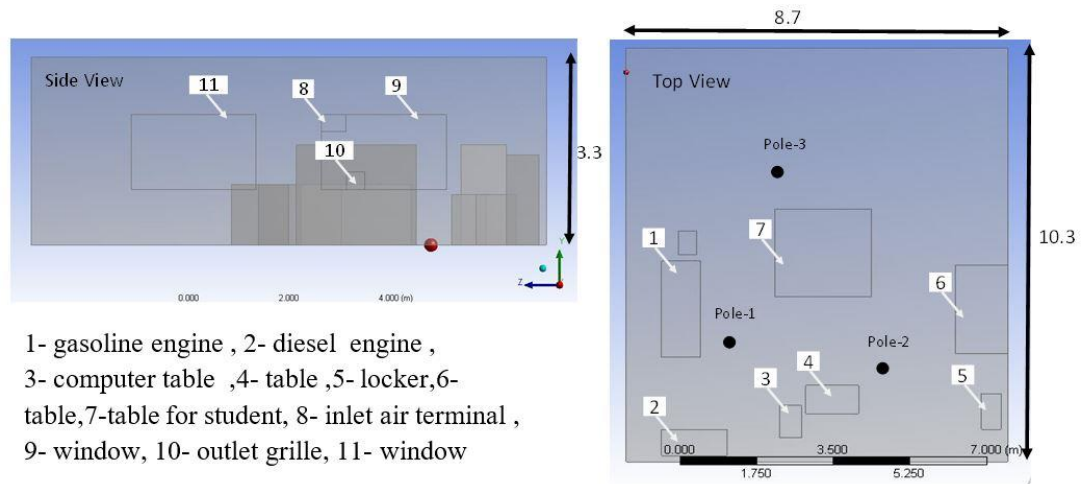


**Fig. 1. The layout of the tested internal combustion engine laboratory and position of sensors.**

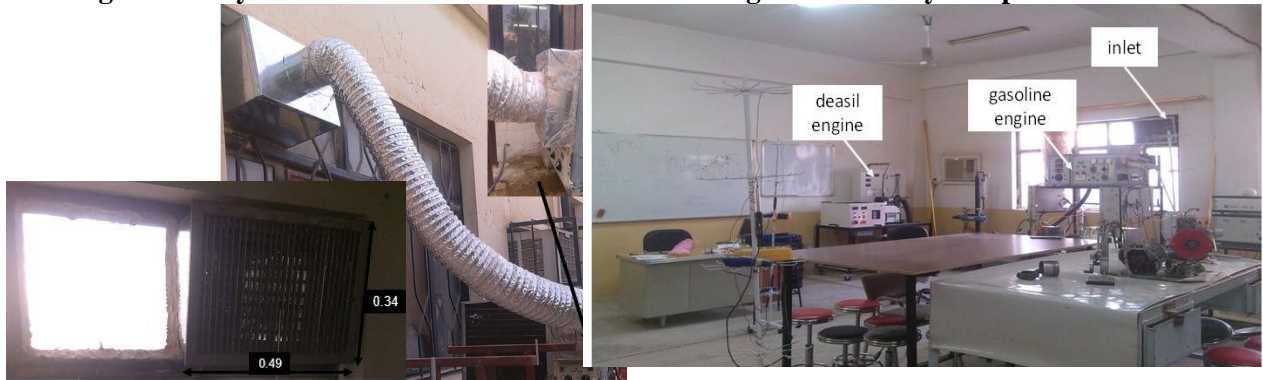


**Fig. 2. Supply air terminal configuration.**

**Fig. 3. Selected internal combustion engine tested laboratory for measurements.**

### 3. NUMERICAL SOLUTION

#### 3.1. Assumptions

In order to study additional types of chemical pollutants in the studied laboratory, a new variable was introduced in the CFD model. Air was treated as a main liquid and the chemical pollutants introduced (CO<sub>2</sub>, CO and NO<sub>x</sub>) were treated at normal atmospheric pressure. This study assumes that the characteristics of the flow are constant, three-dimensional flow, Newtonian and incompressible, no chemical reactions and turbulent flow.

#### 3.2. Models of turbulence flow

Turbulence model consists of a group of various equations when solved in conjunction with the suitable forms of the momentum and continuity equations, sacrificing the manner of the Reynolds stresses. Many models have been inserted during the years, with varying degrees of success. The success ratio of the model is determined according to the following three criteria.

- 1- Accuracy: The model ought to qualify for providing solution who is within acceptable bounds of reasonable empirical results and the basic governing equation of fluid dynamics.
- 2- Generality: The model ought to be qualified for being perform in a wide variety of flow conditions and geometry without request significant changes.
- 3- Easily Implemented: Although computational capabilities have significantly raise overly, complex models may raise the desired computational time beyond the limits of feasibility (Versteeg and Malalasekera, 1996).

This section discussed two turbulent models (RNG K- $\epsilon$ , SST K- $\omega$ ), Due to little information for use of these models for more than one type of the pollutant indoor occupancy. The two-equation k- $\epsilon$  turbulence model was first developed by Launder and Spalding (1974), which remains as the most widely used turbulence model for a range of engineering flows and is often referred to as the standard k-  $\epsilon$  model.

### 3.2.1. The RNG k- $\epsilon$ model

The RNG k- $\epsilon$  turbulence model is derived from the instantaneous Navier-Stokes equations by using a mathematical technique called "Renormalization Group" (RNG) method. The analytical derivation results in a model with constants, different from those in the standard k- $\epsilon$  model additional terms and functions in the transport equations for k and  $\epsilon$ . The RNG k- $\epsilon$  model is very similar in form to the standard k- $\epsilon$  model. For incompressible flows, the transport equations for k and  $\epsilon$  are as follows (Fluent Inc., 2006),

$$\begin{aligned} \frac{\partial}{\partial t}(\rho k) + \frac{\partial}{\partial x_i}(\rho k u_i) &= \frac{\partial}{\partial x_j} \left[ (\alpha_k \mu_{eff}) \frac{\partial k}{\partial x_j} \right] + G_k + G_b - \rho \epsilon + S_k \\ \frac{\partial}{\partial t}(\rho \epsilon) + \frac{\partial}{\partial x_i}(\rho \epsilon u_i) &= \frac{\partial}{\partial x_j} \left[ (\alpha_\epsilon \mu_{eff}) \frac{\partial \epsilon}{\partial x_j} \right] + C_{1\epsilon} \frac{k}{\epsilon} (G_k + C_{3\epsilon} G_b) - C_{2\epsilon} \rho \frac{\epsilon^2}{k} - R_\epsilon + S_\epsilon \end{aligned} \quad 6$$

Where,  $G_k$  and  $G_b$  terms in the above equations represent the generation of turbulence kinetic energy due to the mean velocity gradients and due to buoyancy, respectively, they are calculated using the equations (7) and (8). The quantities of  $\alpha_k$  and  $\alpha_\epsilon$  are the inverse effective Prandtl numbers for k and  $\epsilon$ , respectively;  $S_k$  and  $S_\epsilon$  are the source terms for k and  $\epsilon$ , respectively.

$$G_k = -\rho \overline{u_i' u_j'} \frac{\partial u_j}{\partial x_i} = \mu_t \left( \frac{\partial u_i}{\partial x_j} + \frac{\partial u_j}{\partial x_i} \right) \frac{\partial u_j}{\partial x_i} \quad 7$$

and  $G_b$  represents the production of turbulent kinetic energy due to buoyancy:

$$G_b = \beta g_i \frac{\mu_t}{\sigma_t} \frac{\partial T}{\partial x_i} \quad 8$$

$g_i$  is the component of the gravitational vector in i-direction, and  $\beta$  is the thermal expansion coefficient defined as:

$$\beta = -\frac{1}{\rho} \left( \frac{\partial \rho}{\partial T} \right)_p \quad 9$$

For an ideal gas, equation (8) reduces to:

$$G_b = -g_i \frac{\mu_t}{\rho \sigma_t} \frac{\partial \rho}{\partial x_i} \quad 10$$

The turbulent (eddy) viscosity  $\mu_t$  is obtained by combining  $k$  and  $\varepsilon$  as follows:

$$\mu_t = \rho C_\mu \frac{k^2}{\varepsilon} \tag{11}$$

$C_\mu$ ,  $C_{1\varepsilon}$ ,  $C_{2\varepsilon}$  and  $C_{3\varepsilon}$  are model coefficients constants and,

$$C_\mu = 0.09, C_{1\varepsilon} = 1.44, C_{2\varepsilon} = 1.92$$

$C_{3\varepsilon}$  is determined from the equation

$$C_{3\varepsilon} = \tanh \left| \frac{v}{u} \right| \tag{12}$$

Where  $v$  is the component of the flow velocity parallel to the gravitational vector and  $u$  is the component of the flow velocity perpendicular to the gravitational vector. The scale elimination procedure in RNG theory results in a differential equation for turbulent viscosity:

$$d \left( \frac{\rho^2 k}{\sqrt{\varepsilon \mu}} \right) = 1.72 \frac{\hat{v}}{\sqrt{\hat{v}^3 - 1 + C_v}} d\hat{v} \tag{13}$$

Where,  $\hat{v} = \mu_{eff} / \mu$ ,  $C_v \approx 100$ .

By integrating equation (13), an accurate description of how the effective turbulence transport varies with the effective Reynolds number (or eddy scale) can be obtained, which allows the model to better handle low-Reynolds number and near-wall flows. The inverse effective Brandt numbers  $\alpha_k$  and  $\alpha_\varepsilon$  are computed using the following formula derived from the RNG theory:

$$\left| \frac{\alpha - 1.3929}{\alpha_0 - 1.3929} \right|^{0.6321} \left| \frac{\alpha + 2.3929}{\alpha_0 - 2.3929} \right|^{0.6321} = \frac{\mu_{mol}}{\mu_{eff}} \tag{14}$$

Where  $\alpha = 1/\sigma k = 1/\sigma \varepsilon = 1/\sigma t$  and  $\alpha_0 = 1.0$ . In the high-Reynolds-number limit ( $\mu/\mu_{eff} \ll 1$ ),  $\alpha_k = \alpha_\varepsilon \approx 1.393$ , that means the effective Brandt numbers for  $k$  and  $\varepsilon$  are about 0.7178.

The main difference between the RNG and standard  $k-\varepsilon$  models lies in the additional term in the  $\varepsilon$  equation given by:

$$R_\varepsilon = \frac{C_\mu \rho \eta^3 \left(1 - \frac{\eta}{\eta_0}\right)}{1 + \beta \eta^3} \frac{\varepsilon^2}{k} \tag{15}$$

Where,  $\eta \equiv \frac{Sk}{\varepsilon}$ ,  $\eta_0 = 4.38$ , and  $\beta = 0.012$

The  $\varepsilon$  equation can be rewritten as:

$$\frac{\partial}{\partial t} (\rho \varepsilon) + \frac{\partial}{\partial x_i} (\rho \varepsilon U_i) = \frac{\partial}{\partial x_j} \left[ (\alpha_\varepsilon \sigma_\varepsilon \mu_{eff}) \frac{\partial \varepsilon}{\partial x_j} \right] + C_{1\varepsilon} \frac{k}{\varepsilon} (G_k + C_{3\varepsilon} G_b) - C_{2\varepsilon}^* \rho \frac{\varepsilon^2}{k} + S_\varepsilon \tag{16}$$

Where  $C_{2\varepsilon}^*$  is given by

$$C_{2\varepsilon}^* = C_{2\varepsilon} + \frac{C_\mu \eta^3 \left(1 - \frac{\eta}{\eta_0}\right)}{1 + \beta \eta^3} \tag{17}$$

In areas where  $\eta < \eta_0$ , the R term makes a positive contribution, and  $C^*2\varepsilon$  becomes greater than  $C2\varepsilon$ . In the logarithmic layer, for instance, it can be displayed that  $\eta \approx 3.0$ , giving  $C^*2\varepsilon \approx 2$ , which is near in magnitude to its value in the standard k- $\varepsilon$  model (1.92). As a result, for weakly to moderately strained flows, the RNG model tends to give results largely comparable to the standard k- $\varepsilon$  model. In sections of great strain rate ( $\eta > \eta_0$ ), however, the R term makes a negative contribution, making the value  $C^*2\varepsilon$  of less than  $C2\varepsilon$ . In comparison with the standard k- $\varepsilon$  model, the smaller destruction of  $\varepsilon$  augments  $\varepsilon$ , decreasing k and, eventually, the effective viscosity. The RNG model yields a lower turbulent viscosity than the standard k- $\varepsilon$  model in rapidly strained flows. Thus, the RNG model is more responsive to the influence of rapid strain and streamline curvature than the standard k- $\varepsilon$  model, which explains the superior performance of the RNG model for certain classes of flows, (Fluent Inc., 2006).

The model constants in equation (16) are the following values:  $C1\varepsilon=1.42$  and  $C2\varepsilon=1.68$ , The coefficient  $C3\varepsilon$  is determined by equation (12).

### 3.2.2. The k- $\omega$ model

The shear stress transport (SST) k- $\omega$  model was developed by Menter to effectively blend the robust and accurate formulation of the k- $\omega$  model in the near-wall region with the free-stream independence of the k- $\varepsilon$  model in the far field. To achieve this, the k- $\varepsilon$  model is converted into a k- $\omega$  formulation. The SST k- $\omega$  model is similar to the standard k- $\omega$  model. These features make the SST k- $\omega$  model more accurate and reliable for a wider class of flows (e.g. adverse pressure gradient flows, airfoils, transonic shock waves) than the standard k- $\omega$  model. Other modifications include the addition of a cross diffusion term in the  $\omega$  equation and a blending function to ensure that the model equations behave appropriately in both the near-wall and far-field zones, (Fluent Inc., 2006).

The SST k- $\omega$  model has a similar form to the standard k- $\omega$  model:

$$\frac{\partial}{\partial t}(\rho k) + \frac{\partial}{\partial x_i}(\rho k u_i) = \frac{\partial}{\partial x_j} \left[ \Gamma_k \frac{\partial k}{\partial x_j} \right] + \tilde{G}_k + -Y_k + S_k \quad 18$$

$$\frac{\partial}{\partial t}(\rho \omega) + \frac{\partial}{\partial x_i}(\rho \omega u_i) = \frac{\partial}{\partial x_j} \left[ \Gamma_\omega \frac{\partial \omega}{\partial x_j} \right] + G_\omega - Y_\omega + D_\omega + S_\omega$$

In these equations,  $\tilde{G}_k$  represents the generation of turbulence kinetic energy due to mean velocity gradients, calculated as described in eq.(4-8) that represents the generation of  $\omega$ , calculated as

$$G_\omega = \alpha \frac{\omega}{k} G_k \quad 19$$

The  $\Gamma_k$  and  $\Gamma_\omega$  represent the effective diffusivity of k and  $\omega$ , respectively, which are calculated as described below.  $Y_k$  and  $Y_\omega$  represent the dissipation of k- $\varepsilon$  and  $\omega$  due to turbulence, calculated as described in the Fluent documentation.  $D_\omega$  represents the cross-diffusion term, calculated as described below.  $S_k$  and  $S_\omega$  are user-defined source terms.

$$\Gamma_k = \mu + \frac{\mu_t}{\sigma_k} \quad 20$$

$$\Gamma_\omega = \mu + \frac{\mu_t}{\sigma_\omega} \quad 21$$

Where,  $\sigma_k$  and  $\sigma_\omega$  are the turbulent Brandt numbers for  $k$  and  $\omega$ , respectively. The turbulent viscosity,  $\mu_t$ , is computed as follows:

$$\mu_t = \frac{\rho k}{\omega} \frac{1}{\max\left[\frac{1}{\alpha^*}, \frac{SF_2}{\alpha_1 \omega}\right]} \quad 22$$

$$\sigma_k = \frac{1}{\frac{F_1}{\sigma_{k,1}} + (1-F_1)/\sigma_{k,2}} \quad 23$$

$$\sigma_\omega = \frac{1}{\frac{F_1}{\sigma_{\omega,1}} + (1-F_1)/\sigma_{\omega,2}} \quad 24$$

The coefficient  $\alpha^*$  damps the turbulent viscosity causing a low-Reynolds-number correction. It is given by:

$$\alpha^* = \alpha_\infty^* \left( \frac{\alpha_0^* + Re_t/R_k}{1 + Re_t/R_k} \right) \quad 25$$

$$Re_t = \frac{\rho k}{\mu \omega} \quad 26$$

$$R_k = 6 \quad 27$$

$$\alpha_0^* = \frac{\beta_i}{3} \quad 28$$

$$\beta_i = 0.072$$

The blending functions,  $F_1$  and  $F_2$ , are given by

$$F_1 = \tanh(\Phi_1^4) \quad 29$$

$$\Phi_1 = \min \left[ \max \left( \frac{\sqrt{k}}{0.09\omega y}, \frac{500\mu}{\rho y^2 \omega} \right), \frac{4\rho k}{\sigma_{\omega,2} D_\omega^+ y^2} \right] \quad 30$$

$$D_\omega^+ = \max \left[ 2\rho \frac{1}{\sigma_{\omega,2}} \frac{1}{\omega} \frac{\partial k}{\partial x_j} \frac{\partial \omega}{\partial x_j}, 10^{-10} \right] \quad 31$$

$$F_2 = \tanh(\Phi_2^2) \quad 32$$

$$\Phi_2 = \max \left[ 2 \frac{\sqrt{k}}{0.09\omega y}, \frac{500\mu}{\rho y^2 \omega} \right] \quad 33$$

Where,  $y$  is the distance to the next surface, and is the positive portion of the cross-diffusion term.

$$D_\omega = 2(1 - F_1)\rho\sigma_{\omega,2} \frac{1}{\omega} \frac{\partial k}{\partial x_j} \frac{\partial \omega}{\partial x_j} \quad 34$$

$$\sigma_{k,1}=1.176, \sigma_{\omega,1}=2.0, \sigma_{k,2}=1.0, \sigma_{\omega,2}=1.168, \alpha_1=0.31, \beta_{i,1}=0.075, \text{ and } \beta_{i,2}=0.0828$$

### 3.3. Description of case study in the internal composition engine laboratory, case-I

The model of test chamber is created in the commercial software ANSYS –Design- Modeler. The geometries and placements of the interior layout were kept as same as they are in the experiment. Applying three cases for case-I, (case-I, a) empirical and numerical study for internal composition engine laboratory with one engine operate, case-I, b numerical study for internal composition engine laboratory with two engine operate and case-I, c for three engine operate. The test hall of the laboratory case with using mixing system ventilation has the inside dimension (10.3 X 8.7 X 3.75) m.

### 3.4. Description of case study in the laboratory of chemical and petroleum products at refinery of Najaf, case-II

This part displays a numerical study of a chemical laboratory in the refinery of Najaf for prognosticating the indoor air flow, thermal comfort and healthy by applying system of mixing ventilation with various locations of supply air terminal. Case-II, a the geometries and placements of the interior layout are kept as same as they are in the actual as shown in Fig. 4, a and case-II, b change the place of the supply air terminal as shown in Fig. 4, b. The inner dimension of test space of the case laboratory with system of mixing ventilation is (3.7 x 3.6 x 3.3)m. Table 3 displays the internal design dimensions of the laboratory and the heat emitted from the apparatus and persons. Using four vertical poles (1, 2, 3 and 4). Each pole has (1.8 m) high and used to discuss the flow of air, temperature distributions, the velocity of air and contaminate concentration in the examined laboratory as displayed in Fig. 4.

### 3.5. Mesh generation

The main tasks in pre-processing are to define the geometry of the computational domain and designate the cells or elements on which the fluid flow equations are solved which are known as domain discretization. The grid has a great impact on the convergence rate, solution accuracy and computing time. An inadequate grid gives poor predictions, while a dense grid demands high computer resources. Skewness is one of the primary quality measures for a mesh. Skewness determines how close to ideal (i.e., equilateral or equiangular) a face or cell is a Table 4. Table 5 shown skewness for cases studied. The quality of the mesh plays a significant role in the accuracy and stability of the numerical computation. Regardless of the type of mesh used in the domain, checking the quality of mesh is essential. One important indicator of mesh quality that ANSYS FLUENT allows checking is a quantity referred to as the orthogonal quality, and the range for orthogonal quality is 0-1, where a value of 0 is worst and a value of 1 is best. Table 6 shown orthogonal quality for cases studied. Figs. 5 and 6 show part of the meshed model for case-I, case-II respectively.

**Table 3. Dimensions and heat convective from components.**

Items	No.	Dimensions (m)			Heat convective(W)
		X	Y	Z	
Door	1	0.2	1	1.5	-
Exhaust	1	0.3	3.7	0.3	-
Lights	31	0.1	0.1	0.25	40
Persons	2	0.4	1.1	0.35	75 per person
Sink	1	0.6	1	1.5	-
Supply-case I	3	0.25	0	0.25	-
Supply-case II	3	0.25	3.7	0.25	-
Table 1	1	2	1	0.6	-
Table 2	1	0.6	1	3	-
Table 3	1	0.6	1	1	-

**Table 4. Skewness ranges and cell quality (Fluent Inc. 2006) [10].**

Value of Skewness	Cell Quality
0	degenerate
< 0.02	bad (sliver)
0.25 - 0.02	poor
0.5 - 0.25	fair
0.75 - 0.5	good
0.75 - 1	excellent
1	equilateral

**Table 5. Values of skewness for cases studied.**

Case study	Value of Skewness
Case-I, a	0.819
Case-I, b	0.848
Case-I, c	0.842
Case-II, a	0.834
Case-II, b	0.84

**Table 6. Values of orthogonal quality for cases studied.**

Case study	Value of orthogonal quality
Case-I, a	0.996
Case-I, b	0.996
Case-I, c	0.996
Case-II, a	0.992
Case-II, b	0.994

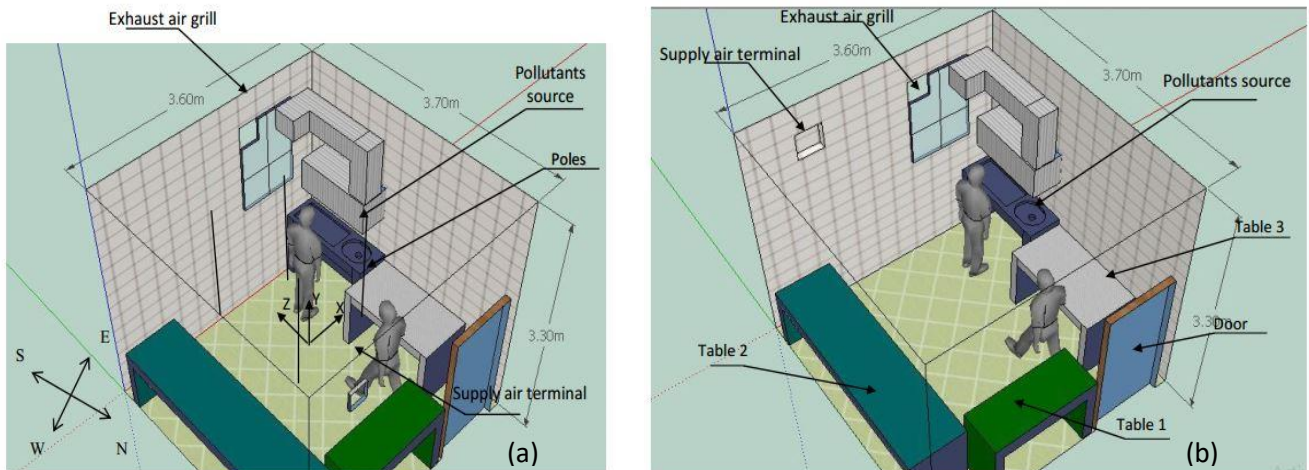


Fig. 4. (a) Schematic diagram for the tested laboratory for case-II,

(b) Schematic diagram for the tested laboratory for case-II,

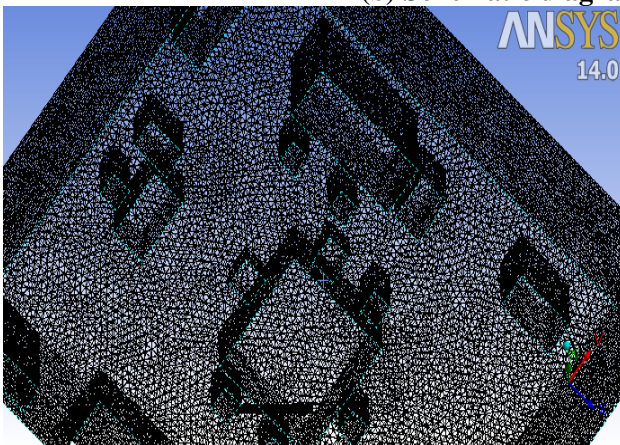


Fig. 5. Part from meshed model, case-I .

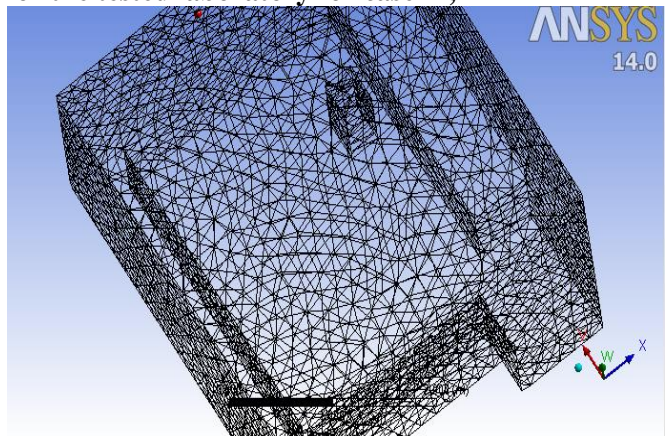


Fig. 6. Part from meshed model, case-II .

### 3.6. Validation and error calculation

It was necessary to validate Fluent software with another experimental study. The validation was done by comparing the RNG k- $\epsilon$  model results with experimental data obtained in a tested room with a wall supply mixing ventilation system. A room of (2.86 X 2.86 X 2.35) m was constructed with an insulated interior surface. A rectangular air inlet 0.39m X 0.24 m was located at one upper corner, and a circular 0.1 m diameter exhaust was located at the diagonally opposite corner of the inlet on the same wall of the room as shown in Fig. 7. A constant flow of the tracer gas (99.5% propylene) was continuously emitted through a 0.1-m screened opening in the top of a 1-m high pedestal located at the center of the room (Khana et al., 2006). The comparison depends on the contaminate concentration resulted which listed in table-1 in Ref (Khana et al., 2006). The comparison gives a good agreement between the experimental and simulated data obtained by the RNG k- $\epsilon$  turbulent model as shown in Fig. 8. The average error between the experimental and numerical values calculated is 6.7 %.

### 3.7. Comparison of practical results with theoretical

Compared between the present practical work and numerical work results which are acquired by using RNG K- $\epsilon$  and SST k- $\omega$  models. It is significant to locate the percentage error between them. The comparison between the numerical and experimental results will be explain in the following part. The Figs. 9 to 12 showed a comparison between the practical and numerical temperature, air velocity, relative humidity and contaminate concentrations results in the I.C laboratory that tested. Fig. 9 shows air temperature distribution results obtained from the two turbulence models (RNG k- $\epsilon$  and SST k- $\omega$ ) for this case from the measuring devices fixed at the three poles. The predicted air temperatures have some deviation with the experimental results, which clearly showed the difference in the temperature curves. The air temperature was generally increased with height due to the buoyancy effect of heat sources and the air temperature under 1.1m height increased more than the top locations of the pole due to the most of the heat source (persons & I.C engine) released under 1.1m. Variations of air temperature between the minimum and maximum points at pole-1 were higher than variations of air temperature at poles 2&3 for the two turbulence models since pole-1 was the nearest to the supply cold air unit. The results displayed that the studied temperature profiles come to an agreement well with the measured data. Fig. 10 shows the results for air velocity distribution obtained from the two turbulence models (RNG k- $\epsilon$  and SST k- $\omega$ ) from the measuring devices fixed at the three poles. The two turbulence models showed the variety in the values of air velocity appeared in the area near the floor level, that was due to the effect of the boundary layer, which was present in knowing that the two turbulence models following the same method of treatment near the walls. Velocity in the occupied zone for the most part under 0.1m/s, with small velocity variations (less than 0.05m/s) along the height for the two turbulence model.

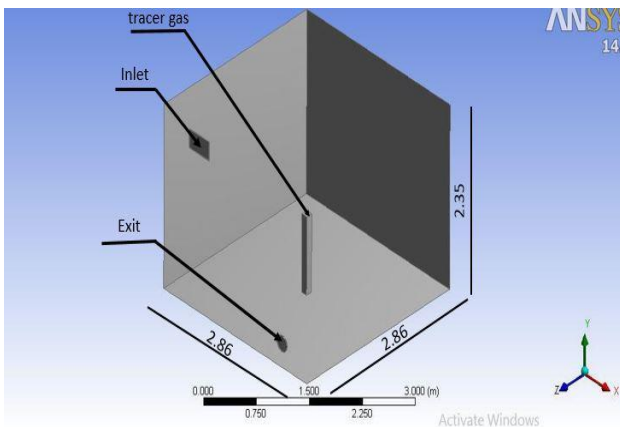


Fig. 7. Schematic diagram for the tested room validation.

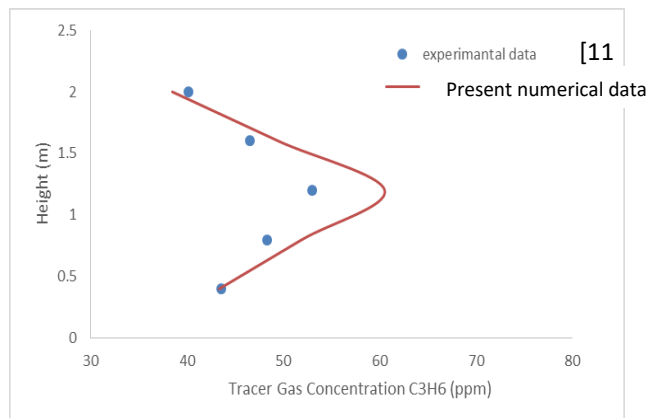
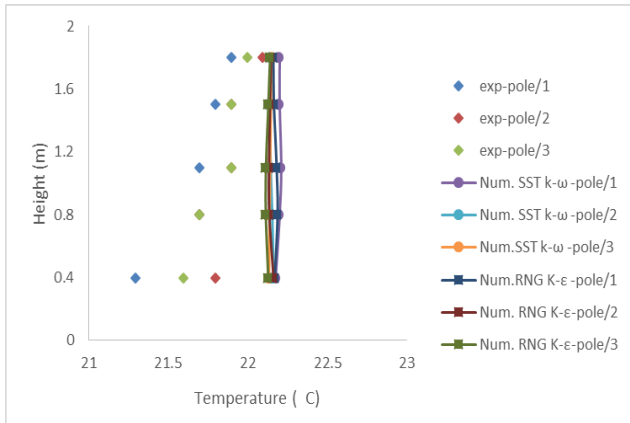
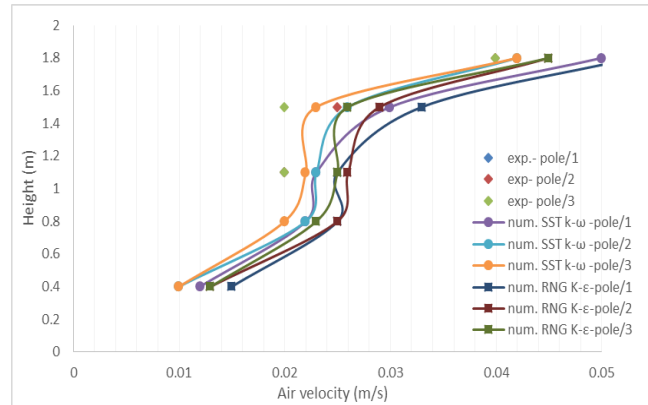


Fig. 8. Validate the RNG K- $\epsilon$  turbulent model with another experimental study (Khana et al., 2006) [11].



**Fig. 9. Comparison between theoretical and empirical results of air temperature with the vertical area in the tested I.C laboratory.**



**Fig. 10. Comparison between theoretical and empirical results of air velocity with the vertical area in the tested I.C laboratory.**

Fig. 11 shows the results for a relative humidity of air distribution obtained from the two turbulence models (RNG k- $\epsilon$  and SST k- $\omega$ ) from the measuring devices fixed at the three poles. The two turbulence models showed the variety in the values of relative humidity appeared in the area near the floor level, that was due to the effect of the boundary layer and the different densities, which was present in knowing that the two turbulence models following the same method of treatment within the occupied zone. Relative humidity in the occupied zone for the most part under 36%, with small relative humidity variations (less than 3%) along the height of the two turbulence model. Fig. 12 shows the results for a contaminant concentration of CO<sub>2</sub> distribution obtained from the two turbulence models (RNG k- $\epsilon$  and SST k- $\omega$ ) from the measuring devices fixed at the three poles. The two turbulence models showed the variety in the values of CO<sub>2</sub> concentration appeared in the area near the floor level, that was due to the different densities between air and CO<sub>2</sub>, which was present in knowing that the two turbulence models following the same method of treatment within the occupied zone. Contaminant concentrations of CO<sub>2</sub> in the occupied zone for the most part under 700 ppm, with relative CO<sub>2</sub> variations (less than 250 ppm) along the height of the two turbulence model, that was agreement with the (ASHRAE Standard, 2001) the CO<sub>2</sub> concentrations should be less than 1000 ppm in the occupied zone. The simulated results compared with the experimental results by calculating the absolute overall error with use of the following equation, [Johnson et al., 2005]:

$$E = \sum_{i=1}^n \left| \frac{X_{CFD}^i - X_{EXP}^i}{X_{EXP}^i} \right| * 100 \quad 35$$

Where X air velocity, air temperature, contaminate concentration and relative humidity.

$|X_{CFD}^i - X_{EXP}^i|$  is the absolute difference between the simulated values and the experimental measurement values for variable X and (n) number of measurements.

Table 7 presents an average error between simulated results for the two turbulence models and the experimental data (15 reading recorded from the three poles) for air (temperature, velocity, relative humidity and contaminate concentration) obtained from Eq. (35).

**Table 7. The average error between simulated and experimental results for the used two turbulence models.**

Turbulent model \ parameter	Error %			
	Temperature	Velocity	Relative humidity	CO <sub>2</sub> concentrations
<b>K-W/SST</b>	1.69	7.2	1.5	10.2
<b>K-E / RNG</b>	1.62	22.8	7.2	11.2

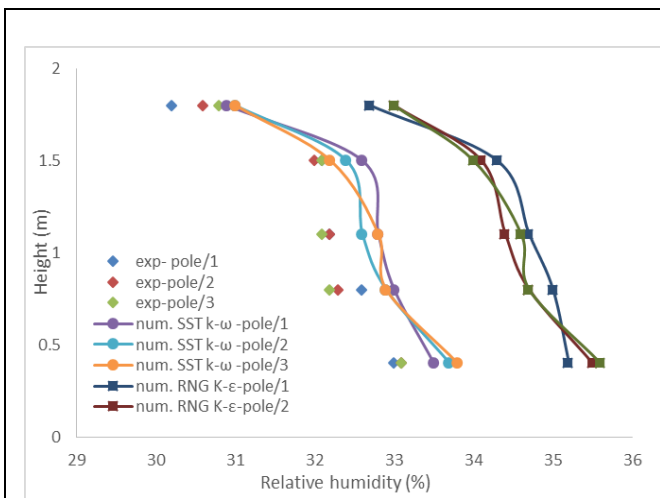


**Fig. 11. Comparison between theoretical and empirical results of air relative humidity with the vertical area in the tested I.C laboratory.**

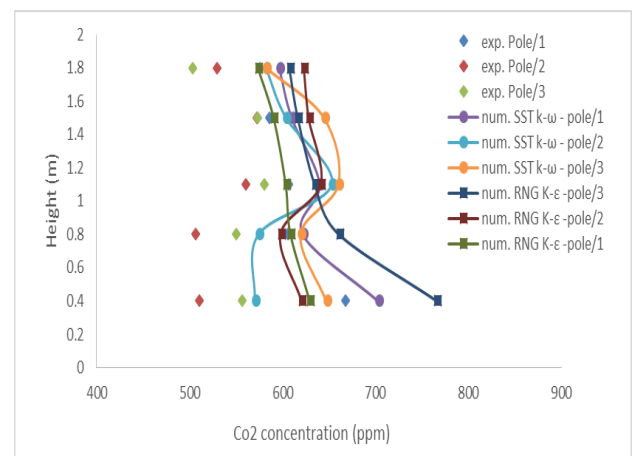


**Fig. 12. Comparison between theoretical and empirical results of CO<sub>2</sub> concentrations with the vertical area in the tested I.C laboratory.**

## 4. RESULTS AND DISCUSSION

### 4.1. Case-I

Fig. 13 displays the measured air temperature distribution in the three poles without using the mixing ventilation for comparison the distribution temperature before starting the I.C engine of the testing and after starting the I.C engine of the testing. Results show the increase in the temperature with the height by 2.5 %. Fig. 14 shows results for air temperature distribution obtained numerically and experimentally at the three poles for the case studied by using the mixing ventilation and starting the I.C engine of the testing until reaching to steady condition. Results show the decrease in the temperature with the height by 14.2 %. There is some deviation between the predicted air temperatures and experimental results, which was clearly the difference in the air temperature curves for the three poles. Air temperature under 1m height was increased more than top locations of the pole since most of the heat source (person & engine) was released under (1m). Generally, the air temperature was increasing along height due to the buoyancy effect of heat sources. Fig. 15 display the calculated air temperature distribution for the case studied the mixing ventilation with two and three I.C engine operation; the figures show the increase in the temperature with the height by (10 % and 10.1%) for two

and three I.C engine respectively. Generally, the air temperature was increasing along height for both cases due to the buoyancy effect of heat sources. The temperature difference from head to foot level was less than 3K as stipulated in ASHRAE. Fig. 16 displays the measured air velocity distribution in the three poles without using the mixing ventilation for comparison the distribution of air velocity before starting the I.C engine of the testing and after starting the I.C engine of the testing. Results show the increase in the velocity with the height by 46 %. Fig. 17 shows results for air velocity distribution obtained numerically and experimentally at the three poles for the case studied by using the mixing ventilation and starting the I.C engine of the testing until reaching to steady condition. Results show the increase in the velocity with the height by 1.1 %, there is some deviation between the predicted air temperatures and experimental results. Fig. 18 display the calculated air velocity distribution for the case that studied the mixing ventilation with two I.C engine operation and three I.C engine operation, the figure shows the increase in the air velocity with the height by (4 % and 6.5%) respectively. Generally, the variations in velocities with height less than 0.04 and maximum velocity less than 0.35 as stipulated in ASHRAE. Fig. 19 displays the measured air humidity distribution in the three poles without using the mixing ventilation for comparison the distribution air humidity before starting the I.C engine of the testing and after starting the I.C engine of the testing. Results show the increase in the humidity with the height by 0.2 %. Fig. 20 shows results for air humidity distribution obtained numerically and experimentally at the three poles for the case studied by using the mixing ventilation and starting the I.C engine of the testing until reaching to steady condition. Results show the decrease in the humidity with the height by 0.7 %. Fig. 21 display the calculated relative humidity distribution for the case studied the mixing ventilation with two I.C engine operation and three I.C engine operation, the figure shows the increase in the relative humidity with the height by (0.4 % and 0.6 %) for respectively. Generally, the variations in relative humidity with height was less than 1% and the maximum values less than less than 0.3 that was agreement with thermal comfort zone. Fig. 22 displays the measured CO<sub>2</sub> concentrations distribution in the three poles without using the mixing ventilation for comparison the distribution of CO<sub>2</sub> concentrations before starting the I.C engine of the testing and after starting the I.C engine of the testing. Results show the increase in the concentrations with the height by 29.5 %. Fig. 23 shows results for CO<sub>2</sub> concentrations distribution obtained numerically and experimental at the three poles for the case studied after starting the mixing ventilation and the I.C engine of the testing until reaching to steady condition and show the decrease in the concentrations with the height by 8.3 %. Fig. 24 display the calculated CO<sub>2</sub> concentrations distribution for the case studied the mixing ventilation with two I.C engine operation and three I.C engine operation, the figure shows the increase in the contaminant concentrations with the height by (1.4 % and 10 %) respectively. The highest percentage concentrations has been observed at pole-3 due to a large distance from supply diffuser (remote areas that are not up to it fresh air) such as corners of the room where the highest concentration recorded about (740 ppm). The relative contaminant concentrations of (CO<sub>2</sub>) variations (less than 30 ppm) along the height that was agreement with the (OSHA Standard) the CO<sub>2</sub> concentrations should be less than 1000 ppm for exposure to 8 hours in the occupied zone. Figs. 22 to 24 displays contours of CO<sub>2</sub> concentrations at a vertical plane at Z=4m and the horizontal plane at 1.5m obtained from the three cases studied using turbulence models SST k- $\omega$  in the three poles. Fig. 25 display the contaminants contours for the case

studied the mixing ventilation with one I.C engine operation, Fig. 26 with two I.C engine operation and Fig. 27 with three I.C engine operation. The high temperature prevents removing more containment of the tested room and low air velocity remain more contaminant inside occupancy. Figures show the increment the concentrations in the upper part from the tested laboratory due to a higher temperature near the ceiling. The highest percentage concentrations has been observed near the ceiling above the air terminal diffuser, where the highest concentrations recorded about (740 ppm), that was agreement with the (OSHA Standard) the CO<sub>2</sub> concentrations should be less than 1000 ppm , for exposure to 8 hours in the occupied zone. The contaminants concentration has a little deviation in the region. On the other hand, the flow in the region for the mixing ventilation is stable. The concentrations are uniform throughout the laboratory.

#### 4.2. Case-II

Fig. 28 display the calculated air temperature distribution in the four poles for the case studied before change location of air supply terminal grille comparison with the case studied after change location of air supply terminal grille and show the decrease in the temperature with the height by 3.87 %. The figures show a rise in temperature at a level below 1.5 meters due to its proximity to the source of heat (the person). Generally, the air temperature was increased along height for both cases due to the buoyancy effect of heat sources and the temperature difference from head to foot level was remain less than 3K as stipulated in ASHRAE. Fig. 29 display the calculated air velocity distribution in the four poles for the case studied before change location of air supply terminal grille comparison with the case studied after change location of air supply terminal grille and show the decrease in the velocity with the height by 1.4%. Generally, the air velocity was stable along height for both cases and remain the maximum velocity less than 0.35 as stipulated in ASHRAE. Fig. 30 display the contaminate concentrations distribution in the four poles for the case studied before changing the location of air terminal supply grille and compared it after change location of air supply terminal grille. This figure shows that the highest percentage concentration has been observed at pole-2 due to near the source of pollutant where the decrease in concentration recorded about between the two cases (3.31% for CO<sub>2</sub>), (1.68% for CO) and about (1.2 % for H<sub>2</sub>S). The relative contaminant concentration of (CO<sub>2</sub>, CO and H<sub>2</sub>S) variations (less than 2 ppm for CO<sub>2</sub>, less than 0.05 ppm for CO and H<sub>2</sub>S) along the height that was agreement with the (OSHA Standard) the CO<sub>2</sub> concentration should be less than 1000 ppm, CO less than 35 ppm and H<sub>2</sub>S less than 10 ppm for exposure to 8 hours in the occupied zone.

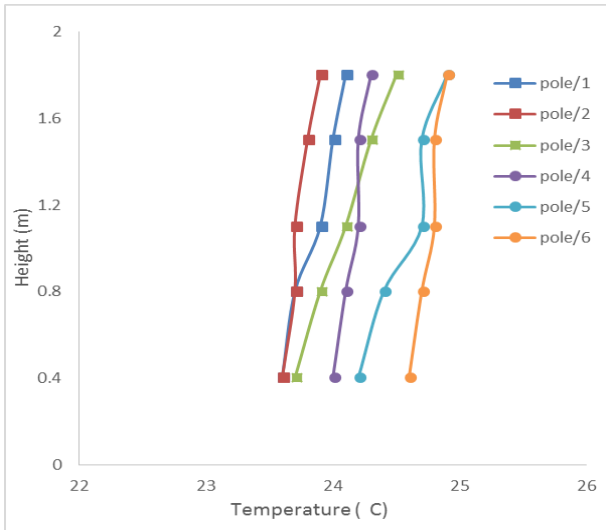


**Fig. 13.** Air temperature distribution before starting the mixing ventilation and the I.C engine for (poles1-3), after starting the I.C engine for (poles 4-6).

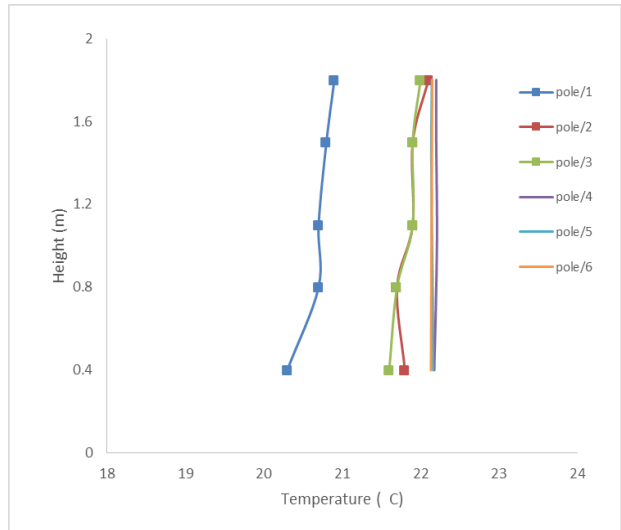


**Fig. 14.** Air temperature distribution after starting the mixing ventilation and the I.C engine, (poles1-3 experimental), (poles 4-6 numerical).

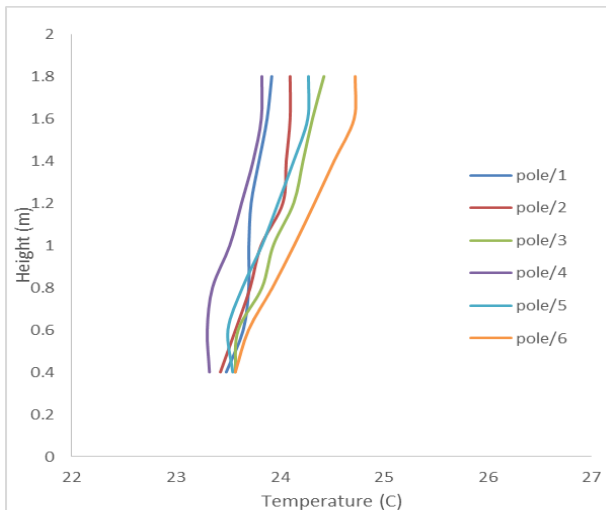


**Fig. 15.** Air temperature distribution for the mixing ventilation with two and three I.C engine operation, (poles1-3 two I.C engine), (poles 4-6 three I.C engine).

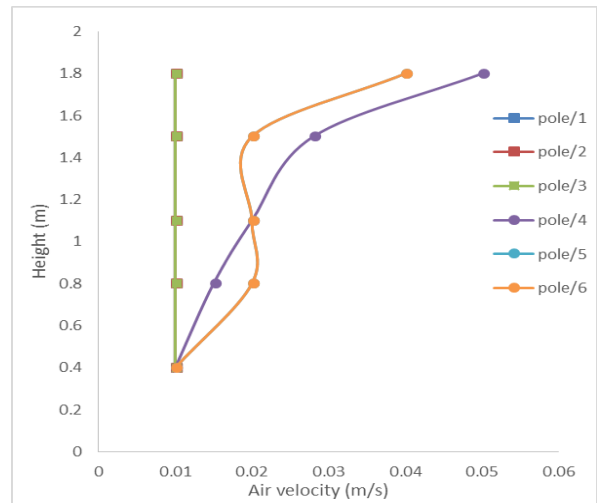


**Fig. 16.** Air velocity distribution before starting the mixing ventilation and the I.C engine for (poles 1-3), after starting the I.C engine for (poles 4-6).

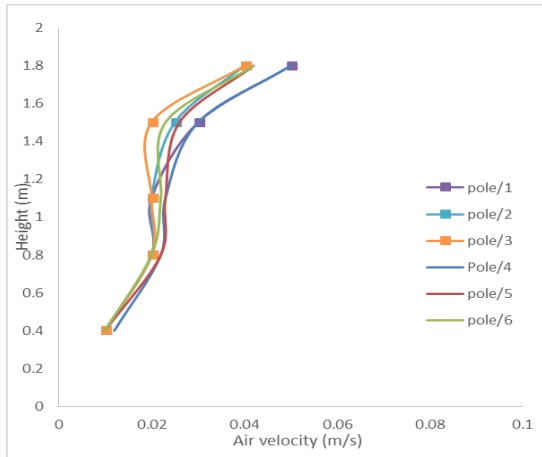


**Fig. 17.** Air velocity distribution after starting the mixing ventilation and the I.C engine, (poles 1-3 experimental), (poles 4-6 numerical).

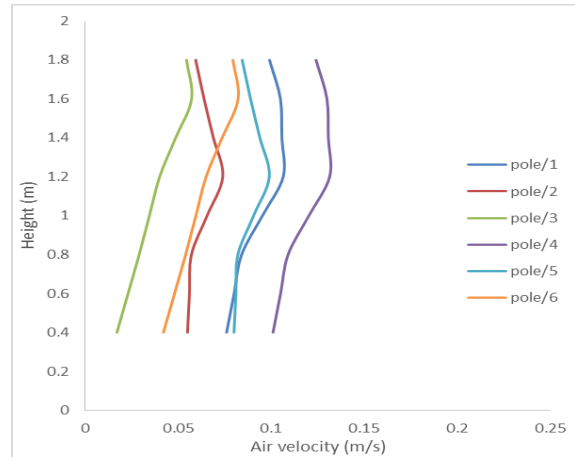


**Fig. 18.** Air velocity distribution for the case studied the mixing ventilation with two and three I.C engine operation, (poles1-3 two I.C engine), (poles 4-6 three I.C engine).

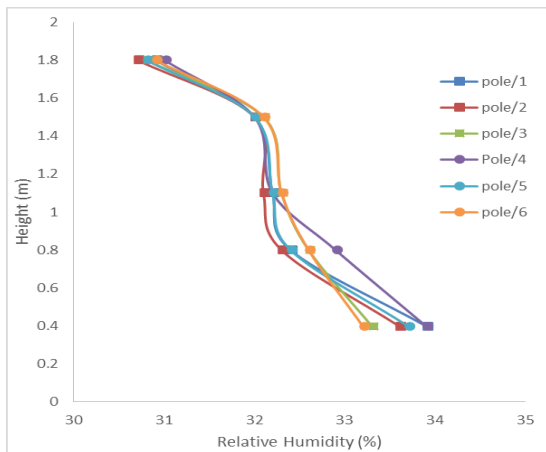


**Fig. 19.** Relative humidity before starting the mixing ventilation and the I.C engine for (poles 1-3), after starting the I.C engine for (poles 4-6).

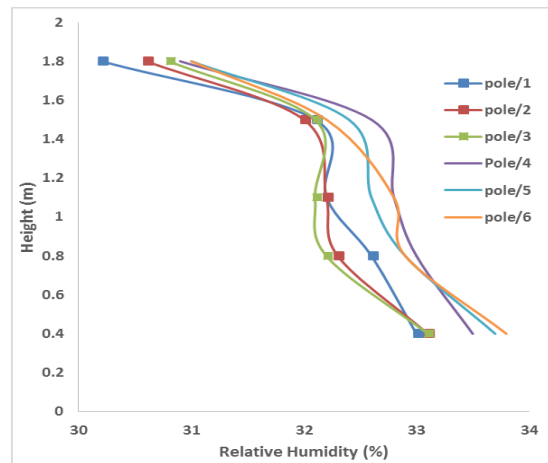


**Fig. 20.** Relative humidity after starting the mixing ventilation and the I.C engine, (poles 1-3 experimental), (poles 4-6 numerical).

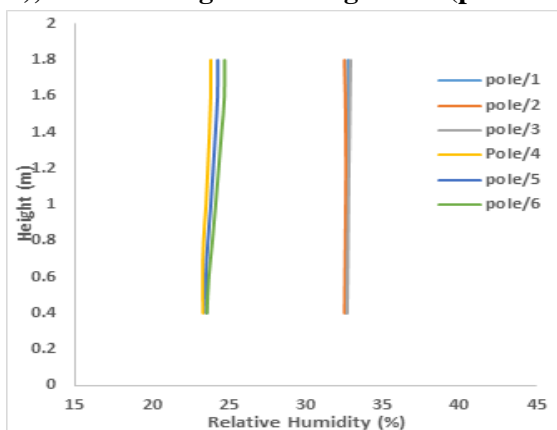


**Fig. 21.** Relative humidity for the mixing ventilation with two and three I.C engine operation, (poles1-3 two I.C engine), (poles 4-6 three I.C engine).

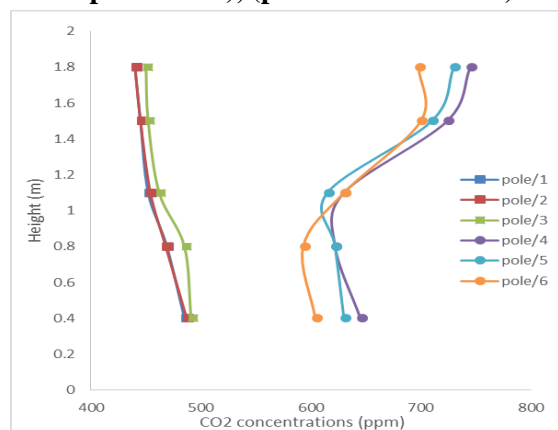


**Fig. 22.** CO2 concentrations before starting the mixing ventilation and the I.C engine for (poles 1-3), after starting the I.C engine for (poles 4-6).

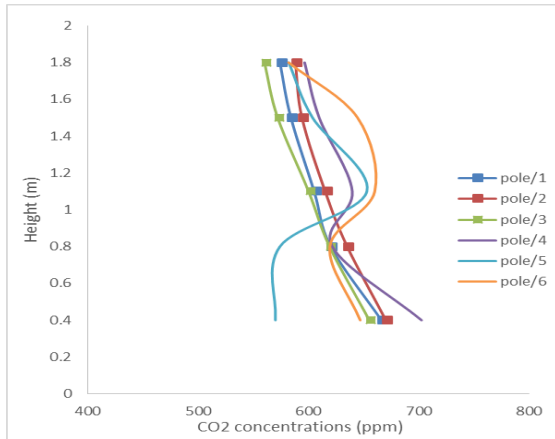


Fig. 23. CO2 concentrations after starting the mixing ventilation and the I.C engine, (poles 1-3 experimental), (poles 4-6 numerical).

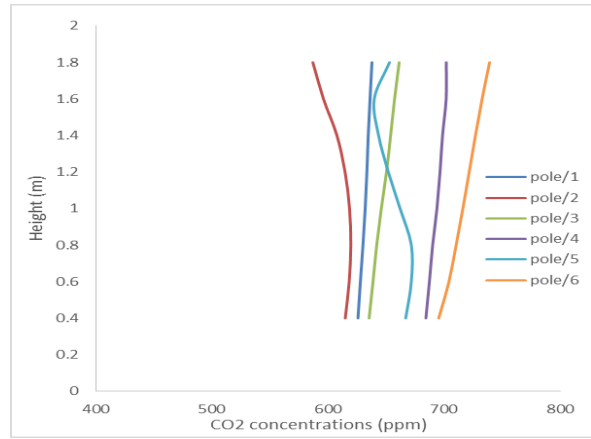


Fig. 24. CO2 concentrations for the mixing ventilation with two and three I.C engine operation, (poles1-3 two I.C engine), (poles 4-6 three I.C engine).

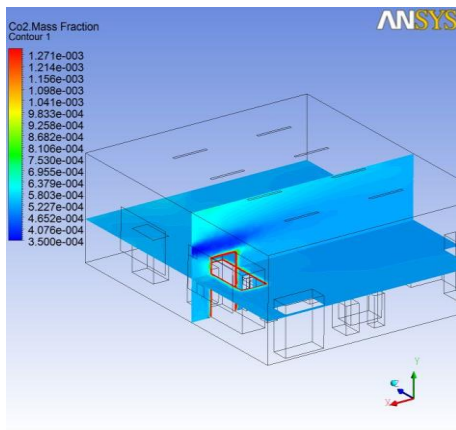


Fig. 25. CO2 concentration in the I.C laboratory for case-1,a at one engine in operation.

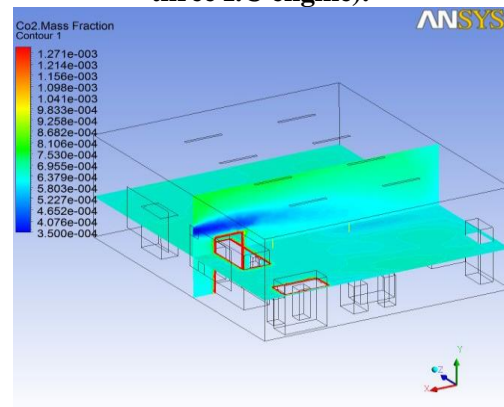


Fig. 26. CO2 concentration in the I.C laboratory for case-1,b at two engines in operation.

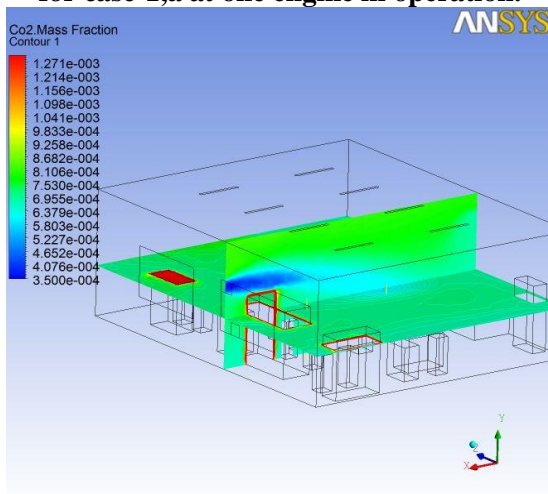


Fig. 27. CO2 concentration in the I.C laboratory for case-1,c at three engines in operation.

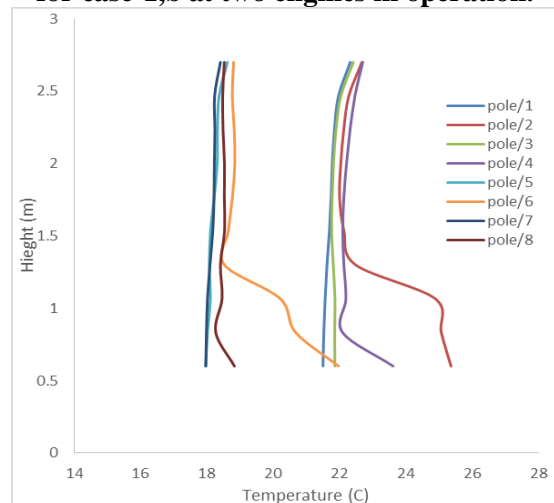
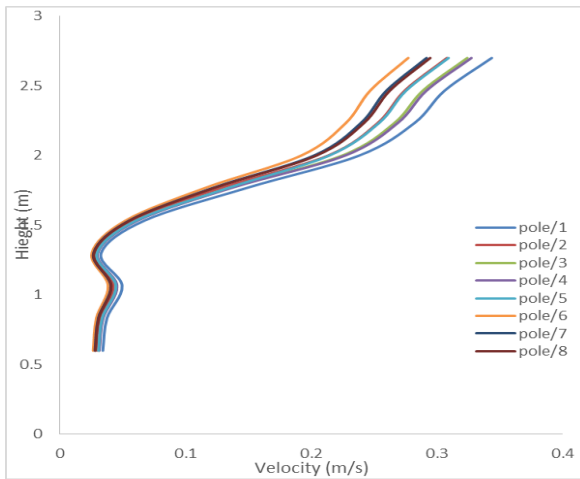
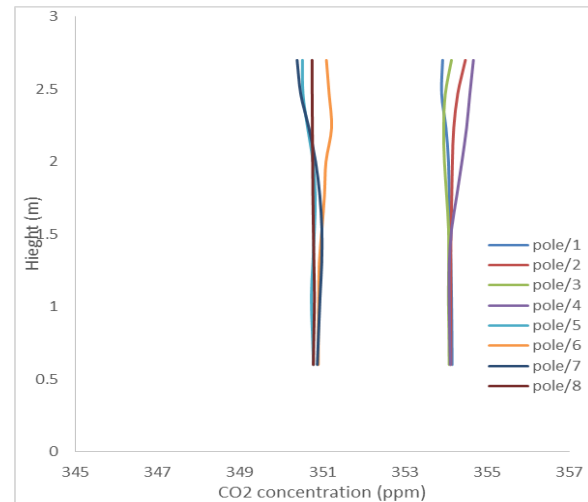


Fig. 28. Air temperature distribution y before change location of air supply terminal grille (poles 1-4), after change location of air supply terminal grille (poles 5-8).



**Fig. 29. Air velocity distribution before change location of air supply terminal grille (poles 1-4), after change location of air supply terminal grille (poles 5-8).**



**Fig. 30. CO2 concentrations before change location of air supply terminal grille (poles 1-4), after change location of air supply terminal grille (poles 5-8).**

## 5. CONCLUSIONS

The major conclusions from this study are summarized as follows:

- 1- Type and location of contaminant source can greatly affect local average contaminants concentration in the breathing zone. However, even if under the worst condition, average concentration in breathing zone was acceptable by adopting mixing ventilation system.
- 2- The comparison between the simulation results and experimental ones can verify the reliability of the computational model and provide a theoretical basis for air organization design.
- 3- The turbulence model SST  $k-\omega$  gives good agreement between the experimental and numerical data when using with more variables at the same time.
- 4- The layout of exhaust opening has a rather small influence on the flow fields unless short circuit of the supply air and stagnancy region occur, while the path of contaminant transportation is greatly affected by the layouts of exhaust inlet so the position of it and the contaminant source should be carefully planned.
- 5- The effects of the arrangement of air terminal diffuser opening on the same side with the exhaust air grille on the average concentration are well evident by the decrease in diffusion field and average concentration for all test cases.
- 6- The exhaust opening should be located in a position where contaminants concentration level is high to reduce the risk of dispersion into the occupied zone.
- 7- The higher velocity causes the incoming air to be better mixed with room air before it is exhausted and accompanied by a decrease in the size of the corner eddies but the speed should be maintained less than 0.35 within the occupied space according to the recommendations of ASHRAE.

## 6. REFERENCE

- Awbi, H. B., 2007. Ventilation Systems: design and performance. Taylor and Francis.
- Boyle and Son R. 1899. Natural and artificial methods of ventilation. London: R. Boyle.
- Butler, W. F. 1873. Ventilation of buildings. New York: D. Van Nostrand.
- Fluent Inc. 2006. Fluent 6.3.26 user's guide.
- Gery Einberg. 2005. Air Diffusion and Solid Contaminant Behavior in Room Ventilation – a CFD Based Integrated Approach. Ph. D., Kungl. Institute of Technology.
- Glicksman, L., and Chen, Q. 2003. System performance evaluation and design guidelines for displacement ventilation. American Society of Heating, Refrigerating and Air-conditioning Engineers.
- Hideyuki Amai, B. Arch., M.E. 2016. Experimental Study on Air Change Effectiveness in Mixing Ventilation. MSc, University of Texas at Austin.
- Hossain, M. A., CHOWDHURY, S. M., ISLAM, M. U., ALAMIN, H. M. 2012. Analysis of Exhaust Gas Emissions in A Diesel Engine Operating With Diesel and Biodiesel Blends. Conference: 6th International Mechanical Engineering Conference & 14th Annual Paper Meet (6IMEC&14APM).
- Iraqi Heating Code. 2013. Ministry of Planning - Central Organization for Standardization and Quality Control, Ministry of Construction and Housing - General Authority for Buildings.
- Johnson Lim Soon Chong, Adnan Husain & Tee Boon Tuan. 2005. Simulation of airflow in lecture rooms. proceedings of the AEESAP international conference.
- Khana, J. A., Feigley, C. E., Lee, E., Ahmed, M. R. and Tamanna, S., 2006. Effects of inlet and exhaust locations and emitted gas density on indoor air contaminant concentrations. Building and Environment 41 pp. 851–863.
- Versteeg, H., Malalasekera, W., 1995. An introduction to computational fluid dynamics: the finite volume method (first published). Longman group LTD.